PAPER

Check for updates

Colloidal synthesis of emission-tunable Cu-doped Zn–In–Se/ZnSe core/shell nanocrystals for lighting and bioimaging applications†

Joicy Selvaraj, [iD] [a] Arun Mahesh,[b] Arunkumar Dhayalan,[b]
Vaseeharan Baskaralingam,[c] Saravanan Rajendran, [iD] [d]
Miguel Ángel Gracia Pinilla[e] and Thangadurai Paramasivam [iD] *[a]

Herein, environmentally benign Cu^I:Zn–In–Se/ZnSe core/shell luminescent inorganic nanocrystals (NCs) were synthesized *via* a phosphine-free one-pot, two-step organometallic approach with good colloidal quality. Firstly, Cu^I ion-doped Zn–In–Se colloidal NCs were synthesized *via* a one-pot heating chemical method using phosphine-free, highly reactive alkylammonium selenide as a Se source. The resulting Cu^I-doped Zn–In–Se colloidal NCs exhibited a doping concentration-dependent colour tunable emission in the range of 450–800 nm with a poor emission intensity. Consequently, in the second, to improve the stability and emission intensity of the doped colloidal NCs, a ZnSe shell was grown over their core *via* a hot-injection chemical route. The shell growth, performed at a relatively high temperature of ~240 °C with zinc precursor injection, initially leads to the diffusion of Zn^{II} ions into the core lattice, followed by the partial substitution with Cu^I and In^{III} ions close to the surface of NCs and formation of a shell layer over the core. In addition, a continuous blue shift with an increase in the intensity of the emission peak of core Cu^I:Zn–In–Se NCs, caused by partial cation exchange, was observed after sequential Zn precursor injections at specified intervals. The prolonged radiative lifetime of the NCs was observed with the successive injection of the shell precursor, reaching the highest value of 348.7 ns. Subsequently, the potential application of these Cu^I:Zn–In–Se/ZnSe core–shell NCs in flexible electronics and live-cell imaging was tested. Flexible nanocomposite films of polymer–NCs were prepared *via* the solution drop-casting technique. The composite films showed a good level of optical transmission in the visible region and good PL emission intensity. Moreover, cytotoxicity and optical live-cell imaging studies were carried out and the results revealed that the 11-mercaptoundecanoic acid-capped Cu^I:Zn–In–Se/ZnSe core–shell NCs are biocompatible with the potential for use in the bio-imaging application as a luminescent agent.

[a] *Centre for Nanoscience and Technology, Pondicherry University, Puducherry – 605 014, India. E-mail: thangaduraip.nst@pondiuni.edu.in, thangadurai.p@gmail.com*
[b] *Department of Biotechnology, Pondicherry University, Puducherry – 605 014, India*
[c] *Department of Animal Health and Management, Alagappa University, Karaikudi – 630 003, Tamil Nadu, India*
[d] *Faculty of Engineering, Department of Mechanical Engineering, University of Tarapacá, Avda, General Velasquez, 1775, Arica, Chile*
[e] *Universidad Autónoma de Nuevo León, Faculated de Ciencias Fisico-Matemáticas, Av. Universidad, Cd. Universitian, San Nicolás de los Garza, N.L. 66450, Mexico*

† Electronic supplementary information (ESI) available: The supplementary information file contains additional data that supports and is required for understanding the discussion presented in the main text. Additional data includes XRD, TEM analysis, XPS, fluorescence emission data, digital images of the composite and their emission spectra, and PL of core/shell structure before and after ligand exchange, such as XRD. It contains eight figures and one table providing fitting PL parameters. It also provides the equations used to fit the TRPL time decay profile to get the average lifetime of the PL emission. See DOI: https://doi.org/10.1039/d4lf00132j

1. Introduction

Over the past two decades, colloidal semiconductor nanocrystals (NCs) with a size in the range of their Bohr excitonic radius have emerged as some of the leading dispersed emissive materials owing to their unique combination of optoelectronic properties, which are pronounced by the size quantization effect. Among the various NCs, zero-dimensional semiconductor NCs show great potential in a variety of photon-emitting and photon-harvesting applications, including light-emitting diodes, biomedical fluorophores, luminescent solar concentrators, and photovoltaics.[1–9] In recent years, considering the environmental, health, and safety perspectives, the search for semiconductor NCs containing non-toxic elements with excellent optical properties has highly intensified to replace traditional toxic NCs. Over the course of time, greener I–III–VI$_2$ (for instance, M$_1$M$_2$X; M$_1$ = Cu and Ag; M$_2$ = In; X = S and

© 2024 The Author(s). Published by the Royal Society of Chemistry

RSC Appl. Interfaces, 2024, **1**, 1317–1333 | **1317**

Se) ternary semiconductor compounds have been widely investigated and continuously proven to be promising alternative luminescent materials to toxic binary NCs.[10,11] Besides, eco-friendly Zn-based II–III–VI ternary alloy NCs have attracted significant attention recently. Unfortunately, unlike traditional Cd/Pb- and ternary/quaternary I–III–VI$_2$-based NCs, Zn-based ternary semiconductor NCs do not possess size- and composition-tunable photoluminescence covering the complete visible range. Early studies have demonstrated that the incorporation of transition metal elements into the host lattice of II–III–VI ternary NCs is a promising method for altering their energy transfer processes, thus yielding a tunable emission over a wide spectral range with a large Stokes shift and, consequently, reduced self-absorption.[12–15] Further, ternary chalcogenide semiconductor materials can act as promising hosts for dopant ions because of their composition-dependent optical and electronic properties. For instance, doping Cu$^+$ ions in Zn–In–Se alloy NCs yielded a broad tunable photon-emission in the range of 565 to 710 nm by varying the molar ratio of Zn to In.[13] Ag$^+$-doped Zn–In–S NCs synthesized via a one-pot heating method showed a tunable emission in the range of 392–543 nm by varying the dopant Ag$^+$-ion concentration.[12] In another study, doped ternary alloy NCs of Ag$^+$:Zn–In–Se were synthesized in aqueous solution with a tunable emission in the range of 504 nm to 585 nm by altering the molar ratio of In/Zn in the host.[15] In the spectrum of the doped NCs, their absorption and photon emission regions were well separated compared to the undoped NCs with particle-size dependent emissions.[16,17] This large Stokes shift is a significant feature for fluorescence-based applications, given that it suppresses self-luminescence quenching due to the reabsorption and/or fluorescence resonance energy transfer between the NCs.

In colloidal NCs, the organic capping ligand molecules mainly stabilize the colloidal dispersion of NCs in various solvents by steric hindrance. However, they are too labile to shield the surface of NCs against continuous photo and chemical degradation. Accordingly, a straightforward strategy to overcome these issues in NCs is the deposition of a protective shell of a second inorganic semiconductor material around their crystalline core, i.e., the construction of NCs with a core/shell (C/S) geometry.[18–21] This approach significantly improves the stability and optoelectronic properties of the NC core, with an alloyed core or graded interfacial layer providing the greatest enhancement. Furthermore, due to their wide direct bandgap and stability, the eco-friendly II–VI chalcogenides ZnS (E_g = 3.6 eV) and ZnSe (E_g = 2.7 eV) have been used as shell materials on different core materials to improve their emission characteristics.[14,22,23]

Transition metal ion-doped II–III–VI material systems such as Ag:Zn–In–S, Cu:Zn–In–S, Cu,Mn:Zn–In–S, Ag,Mn:Zn–In–S, Cu:Zn–In–Se and Ag:Zn–In–Se have been developed for various applications.[12,13,15,22,24–28] Recently, our group developed C/S NCs of Ag-doped Zn–In–S/ZnS with tunable emission and fabricated flexible polymer composite films by incorporating Ag-doped NCs in the polymer matrix for

lighting applications.[12] In the literature, Ag,Mn co-doped Zn–In–S/ZnS C/S NCs were as a ratiometric temperature sensor with dual emission[28] and Ag-doped Zn–In–S/ZnS NCs with a QY of 28% and fluorescence lifetime of 309 ns were used to fabricate a white light-emitting diode with a color rendering index of 90.3.[24]

However, despite the numerous reports in this field, studies on transition metal-doped Zn–In–Se NCs are scarce in the literature. Therefore, it is important to develop eco-friendly transition metal-doped Zn–In–Se NCs and understand their optoelectronic properties to realize their potential application. Motivated by this, in the present study, we report the synthesis of pristine and Cu^I-doped Zn–In–Se alloy core NCs as well as Cu^I:Zn–In–Se/ZnSe C/S NCs via the colloidal chemical route with improved emission characteristics for use in optical applications. Here, the Cu^I ion was chosen as the primary luminescent centre and introduced in the lattice of the mother alloy Zn–In–Se to modulate the electronic energy levels of the NCs to yield a tunable emission down to 800 nm with a large Stokes shift to avoid self-absorption. Subsequently, to improve the stability of the NCs and their optoelectronic properties, a ZnSe shell was grown over the Cu^I-doped Zn–In–Se alloy core NCs. The prerequisite characteristics of these NCs for optoelectronic and biological applications were studied to scrutinize their potential in these applications. Furthermore, polymer-core/ shell NC mixed nanocomposite films were prepared by dispersing the hydrophobic Cu^I:Zn–In–Se/ZnSe C/S NCs into a highly transparent organic thermoelectric polymer, polymethyl methacrylate. These nanocomposite films exhibited good emission characteristics, transparency, and mechanical flexibility. Further, to explore their potential for biological applications, the hydrophobic ligand of Cu^I:Zn–In–Se/ZnSe NCs was replaced with the hydrophilic ligand of 11-mercaptoundecanoic acid and applied in live cell imaging (in vitro) as fluorescent agents. The results demonstrated that these NCs are promising for application in optoelectronics and live-cell imaging.

2. Experimental

2.1. Chemicals and reagents

All chemicals used in this work were analytical grade reagents and procured from commercial suppliers with following purity: zinc acetate dihydrate (Zn(OAc)$_2$·2H$_2$O, 98%, HiMedia), indium(III) chloride (InCl$_3$, 98%, HiMedia), selenium powder (Se, 100 mesh, 99%, Sigma-Aldrich), copper(II) acetate monohydrate (Cu(OAc)$_2$·H$_2$O, 98%, Merck), oleylamine (OLA, 70%, Sigma-Aldrich), 1-docecanethiol (1-DDT, ≥98%, Sigma-Aldrich), 1-octadecene (1-ODE, ≥91%, Merck), polymethyl methacrylate (PMMA, molecular weight-120 000, Sigma-Aldrich), 11-mercaptoundecanoic acid (11-MUA, 95%, Sigma-Aldrich), tetramethyl ammonium hydroxide pentahydrate (TMAHP, 97%, HiMedia), chloroform (CHCl$_3$, ≥99%, Merck), acetone (C$_3$H$_6$O, ≥99%, Merck) and methyl alcohol (CH$_3$OH, ≥99%, Merck).

2.2. Synthesis procedures

Initially, colloidal hydrophobic Cu^I:Zn–In–Se core-only NCs were synthesized *via* a one-pot heating method, followed by the deposition of ZnSe shell layers over the core NCs *via* the hot-injection route.[12] The five representative Cu^I:Zn–In–Se/ZnSe C/S NCs with different Cu ion dopant concentrations (0.00, 0.01, 0.02, 0.04, and 0.08 mmol copper precursor concentration) were synthesized by varying the amount of Cu(OAc)$_2$·H$_2$O precursor and keeping the concentration of the other elements (Zn^{2+}, In^{3+}, and Se^{2-}) constant. The synthesis procedure is briefly described below.

2.2.1. Synthesis of colloidal inorganic Cu^I-doped Zn–In–Se alloy core NCs. In the first step of the process for the synthesis of the Cu^I:Zn–In–Se core NCs, the precursors 0.2 mmol Zn(OAc)$_2$·2H$_2$O, 0.2 mmol InCl$_3$, required amount of Cu(OAc)$_2$·H$_2$O and 1.6 mmol elemental Se powder were mixed with 6 mL of OLA and 4 mL of 1-DDT in a three-neck round-bottom flask under vigorous stirring. The flask was equipped with a reflux condenser and a thermometer, and the set-up was placed on a silicone oil bath with a hot-stirring plate. Subsequently, the reaction temperature was gradually increased to 220 °C and maintained at this temperature for 30 min under argon bubbling with constant stirring. The resulting colloidal solution was naturally cooled to room temperature to complete the reaction. For the purification process, the NC colloids were repetitively precipitated by an addition of excess C$_3$H$_6$O, centrifuged, decanted, and redispersed in CHCl$_3$. The purification process was repeated at least three times by adding CHCl$_3$ to disperse the NCs and C$_3$H$_6$O for their precipitation. Finally, the resultant solid NCs were dispersed in CHCl$_3$ solvent and/or dried at 60 °C under vacuum conditions.

2.2.2. Preparation of Zn stock solution for the shell growth. The zinc precursor was prepared by dissolving 2.4 mmol of Zn(OAc)$_2$·2H$_2$O in a mixture of OLA and 1-ODE (v/v, 1:9, in 6 mL) at 140 °C under argon bubbling. This solution was used as the Zn source for the shell growth during the hot-injection method.

2.2.3. Deposition of ZnSe shell layer over the Cu^I-doped Zn–In–Se core NCs. Typically, after the reaction mixture of the core NCs was maintained at 220 °C for 30 min (Section 2.2.1), the temperature of the solution was increased to 240 °C. Instantly, upon reaching this temperature (240 °C), 2 mL of Zn precursor stock solution was quickly injected into the reaction vessel containing the above-mentioned mixture. This sequence was repeated three times with a waiting period of 15 min between each injection. During the reaction, aliquots were collected from the reaction vessel before each consecutive injection of the Zn precursor stock solution and cooled in 3 mL of CHCl$_3$ to quench the growth of the NCs. Once the final reaction was completed, the solution was naturally cooled to room temperature. The purification process was similar to the purification of the core NCs described in Section 2.2.1. Finally, the purified C/S NCs were re-dispersed in CHCl$_3$ and/or dried at 60 °C under vacuum.

2.3. Material characterization techniques

For crystal structure analysis, the XRD patterns of the NCs were acquired using a Rigaku Ultima-IV X-ray diffractometer using Cu-K$_\alpha$ radiation with a wavelength of 1.5406 Å in the θ–2θ Bragg–Brentano geometry. The specimen for microstructure analysis by transmission electron microscopy (TEM) was prepared by depositing the colloidal NCs, dispersed in chloroform solvent, on a 300-mesh copper grid containing an amorphous carbon support thin film, and then the solvent was evaporated by drying at room temperature. The high-resolution TEM micrographs were acquired using a Tecnai G2 F30 S-Twin (FEI) TEM microscope operated at an accelerating voltage of 300 kV. UV-vis absorption spectra were recorded on a Shimadzu, UV-3600 plus spectrometer in the wavelength range of 250 to 800 nm with 1 nm resolution. A Horiba Jobin Yvon (Fluorolog-FL3-11) spectrofluorometer containing a time-correlated single-photon counting (TCSPC) system was used to measure the room temperature steady-state emission spectra and nanosecond transient time-resolved PL (TRPL) decay curves. A xenon arc-lamp and a nanoLED source (290 and 460 nm) were utilized as the excitation sources for measuring the steady-state fluorescence spectra and TRPL decay curves, respectively. The relative quantum yield of the core and core/shell NCs was measured using rhodamine B dye as a reference. The UV-Vis absorbance spectra of the sample dispersed in chloroform solvent and the dye were recorded first and the absorbance at the excitation wavelength (430 nm in this case) used was measured for both the sample and dye. Then, their fluorescence spectrum was recorded and the integrated fluorescence intensity was noted. Using eqn (1), the relative QY was estimated, as follows:

$$QY_X = QY_S \frac{I_X}{I_S} \frac{A_S}{A_X} \frac{\lambda_{exS}}{\lambda_{exX}} \left(\frac{n_X}{n_S}\right)^2 \qquad (1)$$

where subscripts S and X refer to the standard and the sample under investigation, respectively, I represents the integrated area of the PL spectrum, A is the optical density at the excitation wavelength used for the PL measurement (optical density was kept at ~0.05 for all the samples to avoid reabsorption), λ_{ex} is the excitation and n is the refractive index of the solvents (n = 1.4458 for chloroform and n = 1.329 for methanol) (rhodamine B dye in methanol, QY = 70%, emission range: 560–590 nm). The surface chemical oxidation states of the Cu:Zn–In–Se core NCs were investigated through the X-ray photoelectron spectroscopy (XPS) technique (PHI 5000 VersaProbe III, ULVAC-PHI, USA) using Al-K$_\alpha$ monochromatic radiation. The XPS measurement of the Cu:Zn–In–Se/ZnSe C/S NCs was performed using a Kratos AXIS Supra spectrometer (SHIMADZU group, UK) with monochromatic Al-K$_\alpha$ X-ray radiation. The spectra were calibrated with reference to the carbon C-1s peak at 284.8 eV.

2.4. Preparation of polymer–NC composite films

Optically transparent, flexible polymer–NC composite films were prepared by drop-casting the composite solution on

© 2024 The Author(s). Published by the Royal Society of Chemistry

RSC Appl. Interfaces, 2024, **1**, 1317–1333 | **1319**

glass substrates.[12] Four polymer–NC composite films were prepared by mixing PMMA polymer with 0.01 mmol (λ_{em} = 542 nm), 0.02 mmol (λ_{em} = 557 nm), 0.04 mmol (λ_{em} = 585 nm) and 0.08 mmol (λ_{em} = 633 nm) of Cu^I–Zn–In–Se/ZnSe C/S NCs. In a typical process, 10 mg of the dried powder of C/S NCs was dispersed in 5 mL chloroform to get a clear colloidal solution. Simultaneously, 0.5 g of PMMA in pellet form (MW-120 000) was dispersed in 5 mL chloroform under constant stirring at room temperature for 15 min or until the polymer was completely dissolved in the solvent. Subsequently, the clear colloidal NC solution was added to the PMMA solution and left stirring at 40 °C for 30 min. Subsequently, 2 mL of PMMA–NC blend solution was drop-casted on a Petri dish and a glass slide, and finally, they were thermally cured at 50 °C for 2 h in a vacuum. After completion of the curing process, the PMMA–NC thick films were peeled off from the Petri dish, while the films coated on glass slides were used for further measurements. For comparison, bare PMMA films were also prepared *via* a similar method without the C/S NCs. The optical transmittance of the films was assessed using a UV-vis spectrometer (Shimadzu, UV-3600 plus) in the wavelength range of 200 nm to 800 nm using air as the reference. The fluorescence spectra of the films were recorded using a Horiba Jobin Yvon (Fluorolog-FL3-11) spectrofluorometer to study their emission properties.

2.5. Preparation of water-dispersible hydrophobic Cu^I:Zn–In–Se/ZnSe C/S NCs by ligand-exchange method

The exchange of the native hydrophobic ligands on the surface of the prepared C/S NCs by the 11-MUA hydrophilic ligand was achieved as follows.[29] In the first step of the ligand exchange process, 100 mg of 11-MUA was dissolved in 1 mL of CH$_3$OH, and subsequently, the pH of the solution was adjusted to ~12 by adding the organic base TMAHP. Next, 1 mg of purified C/S NCs, in powder form, was dispersed in 1 mL CHCl$_3$ to obtain a homogeneous colloidal solution. Then, the NC solution was swiftly added to the 11-MUA–CH$_3$OH mixture solution and stirred vigorously for 30 min at room temperature. Later, the reaction mixture was heated at 70 °C for 20 min and allowed to cool to room temperature. Once room temperature was achieved, 2 mL of deionized water was added to the mixture and stirred for 10 min. The C/S NCs switched their location from the bottom organic phase to the aqueous phase at the top of the solution. The aqueous phase containing 11-MUA-capped C/S NCs was collected and purified with acetone. The resultant pellet was re-dispersed in 1 mL deionized water/phosphate-buffered saline (PBS, pH 7.4) and stored in a refrigerator (4 °C) for further use.

2.6. *In vitro* biocompatibility assay

The *in vitro* biocompatibility of the hydrophilized Cu^I:Zn–In–Se/ZnSe C/S NCs was assayed on two different cell lines, namely, human embryonic kidney 293 cells (HEK293) and cervical cancer cells (HeLa). These cells were procured from the National Centre for Cell Science (NCCS, Pune), India. The respective cells were cultured separately in growth medium (Dulbecco's modified Eagle's medium, DMEM, HiMedia), supplemented with 10% fetal bovine serum (FBS, HiMedia) and 1% L-glutamine–penicillin–streptomycin solution (HiMedia) in a standard incubator with a humidified atmosphere at 5% CO$_2$ and 37 °C.

The *in vitro* cytotoxicity test was performed using the MTT (3-(4,5-dimethylthiazol-2-yl)-2,5-diphenyltetrazolium bromide) calorimetric assay. In a typical procedure,[29] HEK293 or HeLa cells were seeded in a 96-well flat-bottom culture plate (at the density of 1×10^4 cells per well) in DMEM culture medium and allowed to adhere for 24 h. After adhesion, the cells were treated with various concentrations of hydrophilized C/S NCs ranging from 20 to 50, 100, and 200 μg mL^{-1}. As a control test, the cells were treated with medium without the C/S NCs. As a positive control, the drug MG132 (0.5 μg mL^{-1}) was included in the MTT calorimetric assay, which is a potent proteosomal inhibitor known to induce apoptosis.[30] After 48 h of incubation, the medium in each well was discarded and replaced with fresh culture medium (90 μL) and sterile MTT solution (10 μL of 5 mg mL^{-1}). Further, the plate was incubated for 3 h at 37 °C until the emergence of purple formazan crystals. Thereafter, the unreduced MTT solution was replaced with 100 μL of dimethyl sulfoxide (DMSO, HiMedia) to solubilize the purple formazan crystals. The absorbance of the formazan crystals at 570 nm was measured spectrophotometrically using a microplate reader to determine the optical density (OD) value. The assay was repeated three times, and the results were averaged (±S.D) to get better accuracy. The cytotoxicity effect is expressed as a percentage of cell viability relative to the control cells and is defined as:

$$\text{Cytotoxicity } (\%) = \frac{[\text{OD of NCs treated cells}]_{570\,\text{nm}}}{[\text{OD of control cells}]_{570\,\text{nm}}} \times 100 \qquad (2)$$

2.7. *In vitro* bioimaging

Based on the biocompatibility test results, the hydrophilized Cu^I:Zn–In–Se/ZnS C/S NCs with 100 μg mL^{-1} concentration were used for the cellular uptake study. The specimen for this study was prepared by following the reported procedure.[29] Briefly, HEK293/HeLa cells were cultured in a cell-culture dish with aseptic coverslips in a growth medium for 24 h. Thereafter, the cells were treated with the hydrophilized C/S NCs (100 μg mL^{-1}) and incubated for 6 h at 37 °C. The coverslips containing cells were removed, rinsed with PBS three times, fixed with formaldehyde (4%, HiMedia) for 10 min at room temperature, and finally embedded using MOWIOL solution (Sigma-Aldrich). The fluorescence imaging of the adherent cells on the cover slips was performed using a laser confocal microscope system (Carl Zeiss LSM 710, Germany) equipped with a 20× immersion objective lens. A near UV diode laser (λ = 405 nm) was used as the excitation source.

3. Results and discussion

In this study, we report the phosphine-free synthesis of an inorganic Cu^I-doped Zn–In–Se ternary alloy coated with a ZnSe

shell *via* a one-pot heating method followed by a hot-injection organometallic technique. In the literature, Lewis bases such as trioctylphosphine and tributylphosphine have been extensively used to solubilize the chalcogenide components. However, these phosphines are highly toxic, flammable, and corrosive.[31,32] Therefore, the preparation of materials without phosphines is preferred and the focus of research. As an alternative, to avoid these highly toxic phosphines, safe solvents such as oleylamine and dodecanethiol were used in this work. As reported in the literature, the soluble and highly reactive alkylammonium selenide was generated through the reduction of Se powder by an alkylthiol such as DDT in the presence of OLA and alkylammonium selenide was used as a precursor of Se for the synthesis of Se-based NCs.[33,34] C/S NCs without Cu (*i.e.*, pristine Zn–In–Se/ZnSe) were also prepared as a control sample. The transition metal ion Cu(I) was chosen as the dopant to extend the emission of the Zn–In–Se ternary alloy NCs to a wider wavelength range because copper ion species offer a much wider tunability in the visible region depending on the composition of the host.[35–37] The concentration of Cu ions in the C/S NCs in this study is reported based on the initial concentration (mmol) of the precursor employed in their synthesis process. A series of five samples of C/S NCs with varying Cu concentrations was synthesized. During the preparation of the Cu[I]-doped Zn–In–Se core NCs, the color of the reaction solution turned from light-green to dark red upon adjusting the Cu precursor concentration from 0 to 0.08 mmol. For simple reference, the Cu[I]:Zn–In–Se/ZnSe NC series with an increasing Cu concentration in the core was named NCs@A (pristine), NCs@B (0.01 mmol of Cu), NCs@C (0.02 mmol of Cu), NCs@D (0.04 mmol of Cu) and NCs@E (0.08 mmol of Cu). Similarly, the core/shell structures prepared with one, two, and three consecutive shell precursor injections in the core NCs were denoted as batch 1, batch 2, and batch 3, respectively.

3.1. Structural and microstructural studies

The crystallographic structure of the Cu[I]:Zn–In–Se core and Cu[I]:Zn–In–Se/ZnSe C/S NCs was determined by X-ray diffraction measurement. Fig. 1a presents the X-ray diffraction patterns of the pristine and Cu[I]-doped Zn–In–Se core NCs with various dopant concentrations. Given that the host material contains Zn–In–Se, the acquired diffraction patterns of the core NCs are compared with the tetragonal phase of $ZnIn_2Se_4$ (JCPDS card #39-0458). The XRD patterns of all the core NCs contain three broad peaks, which match well with the three major Bragg-reflections at 2θ angles of 27.03°, 44.86°, and 53.2° in the standard diffraction pattern of tetragonal $ZnIn_2Se_4$ corresponding to the (112), (204) and (312) crystal planes, respectively. The width of the diffraction peaks is quite broad, reflecting the small crystallite size of the core NCs.

Fig. 1b presents the diffraction patterns of the Cu[I]:Zn–In–Se/ZnSe C/S NCs (batch 3) containing different Cu ion dopant concentrations in their core. Given that the shell contains ZnSe, their diffraction peaks are compared with the cubic-
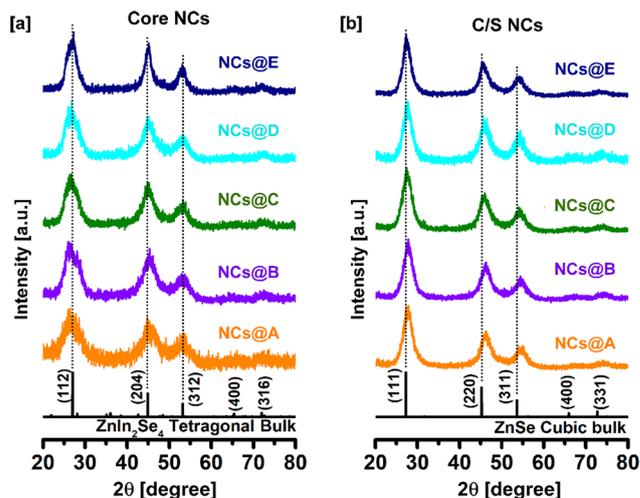

Fig. 1 X-ray diffraction patterns of (a) pristine (NCs@A) and Cu[I]-doped Zn–In–Se (NCs@B to NCs@E) alloy core NCs and (b) pristine Zn–In–Se/ZnSe (NCs@A) C/S NCs and Cu[I]:Zn–In–Se/ZnSe C/S NCs with various Cu dopant concentrations in the core (NCs@B to NCs@E). Stick patterns at the bottom of both figures represent the standard diffraction pattern of tetragonal-structured $ZnIn_2Se_4$ (JCPDS card #39-0458) and cubic-structured ZnSe (JCPDS card #37-1463), respectively.

structured ZnSe (JCPDS card #37-1463). The XRD analysis presented a challenge in distinguishing between the core and shell, given that the major diffraction peaks of $ZnIn_2Se_4$ and ZnSe are located in nearly the same position. However, it can be noted that after injecting 6 mL of Zn precursor solution into the core NCs for the growth of the shell (Experimental section 2.2.3), the Bragg diffraction peaks of the C/S NCs became sharper and significantly shifted to a higher 2θ angle compared to that of the core NCs (Fig. S1 of ESI†). The shift to a high angle in the XRD patterns was observed during the growth of the ZnSe shell on the Cu[I]:Zn–In–Se NCs, corresponding to the formation of the ZnSe shell. The same type of shift in the diffraction peaks was reported in the literature for various metal ion-doped Zn–In–S NCs after encapsulation with a ZnS shell.[24,37] Clearly, the core NCs were formed in one phase, which is tetragonal $ZnIn_2Se_4$. When the (112) peak was observed, it has a less intense minor peak to the right of it, and therefore it appears with a shoulder and slightly broader. However, the (111) peak of the cubic ZnSe phase was sharp and no shoulder appeared. Thus, it was obvious that the ZnSe phase was formed in the shell of the core–shell nanocrystals. Therefore, a phase change from tetragonal $ZnIn_2Se_4$ to cubic ZnSe phase was observed when a shell was grown on the Cu-doped ZnInSe core nanocrystals.

Fig. 2 shows the microstructure results by HRTEM of Cu[I]:Zn–In–Se core NCs (0.04 mmol Cu, NCs@D) and their corresponding C/S NCs (third batch). The colloidal Cu[I]:Zn–In–Se alloy core NCs exhibit a quasi-spherical shape, as shown in Fig. 2a. The HRTEM micrograph of a single nanoparticle chosen from Fig. 2a, as shown in Fig. 2b,
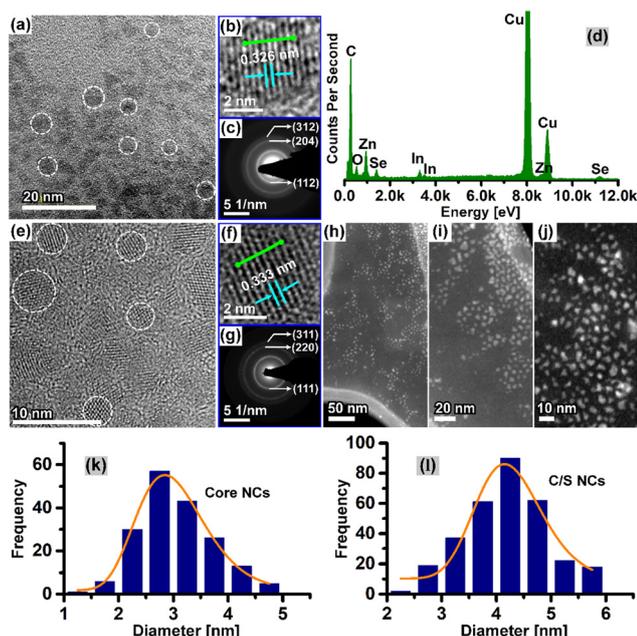
© 2024 The Author(s). Published by the Royal Society of Chemistry

RSC Appl. Interfaces, 2024, **1**, 1317–1333 | **1321**

Fig. 2 (a) Bright-field HRTEM image, (b) zoomed-in HRTEM image of a particle, (c) SAED pattern, and (d) XEDS spectrum of Cu^I-doped Zn–In–Se alloy core NCs. (e) Bright-field HRTEM images, (f) zoomed-in HRTEM image and (g) SAED pattern of Cu^I:Zn–In–Se/ZnSe C/S NCs (batch 3). (h–j) High-angle annular dark-field images of C/S NCs. Particle size distribution histograms of (k) core NCs and (l) corresponding C/S NCs. The histograms are fitted with the log-normal distribution function.

further indicates the crystalline nature of the core NCs through the well-resolved lattice fringe pattern obtained. The intensity line profile, acquired through the selected lattice fringes along the marked green line in Fig. 2b, is presented in Fig. S2a of the ESI.† Between two peaks, the interplanar distance, d, is measured from the x-axis scale. An evenly spaced interplanar distance, d, of 3.26 Å was obtained, which is attributed to the same distance (d = 3.29 Å) of the (112) plane of the bulk tetragonal-ZnIn$_2$Se$_4$. The selected area electron diffraction (SAED) pattern of the Cu^I:Zn–In–Se core NCs, as shown in Fig. 2c, exhibits three distinct concentric circular diffraction rings, with d-spacings of 3.27 Å, 1.94 Å, and 1.66 Å, corresponding to the (112), (204) and (312) reflections (JCPDS card #39-0458), respectively, of tetragonal ZnIn$_2$Se$_4$. The composition analysis by XEDS analysis of the Cu^I:Zn–In–Se core NCs confirmed the presence of Zn, In, Se, and Cu elements, and the typical XEDS spectrum is shown in Fig. 2d. As illustrated in Fig. 2, the bright-field HRTEM micrograph (Fig. 2e) and high-angle annular dark-field micrographs (Fig. 2h–j) of Cu^I:Zn–In–Se/ZnSe C/S NCs indicate that the NCs maintained their shape as nearly spherical even after three sequential shell layers grown *via* Zn precursor injection. The zoomed-in TEM image (Fig. 2f) displays well-defined lattice fringes, which extend in a straight line through the NCs, signifying the good crystallinity of the NCs and the lattice-match with the shell lattice, confirming the epitaxial growth of the ZnSe shell on

the core NCs. Further, the intensity line profile analysis (Fig. S2b of ESI†) of the lattice-resolved TEM image of the C/S NCs revealed that the interplanar spacing of the (111) plane is 3.33 Å. The d-spacings obtained from the SAED pattern of the shell grown Cu^I:Zn–In–Se/ZnSe C/S NCs (Fig. 2g) can be indexed to the crystal planes of cubic ZnSe.

The particle size histogram derived from the of the TEM micrograph analysis of the Cu^I:Zn–In–Se core NCs and the corresponding C/S NCs are presented in Fig. 2k and l, respectively. These histograms were fitted with the log-normal distribution function (orange line profile in Fig. 2k and l). It should be noted that the size distribution for the C/S NCs was determined from their high-angle annular dark-field (HAADF) images. Fig. 2k shows that the doped alloy core NCs grew with a size distribution ranging from 1.5 to 5 nm with an average size of 2.9 ± 0.03 nm. After three consecutive injections of Zn precursor for the growth of the shell, the Cu^I:Zn–In–Se/ZnSe C/S NCs exhibited a larger particle size of 4.2 ± 0.08 nm, with a diameter 1.3 nm greater than that of their mother core NCs.

3.2. XPS analysis

The chemical states of each element in the core and C/S with 0.08 mmol of Cu doping were analyzed by the XPS technique and the results are compared in Fig. 3. The wide-scan photoelectron spectra in Fig. 3a confirm the presence of Zn, In, Cu, and Se chemical elements in both the core and C/S NCs. Further, the signals from the region of the Cu-2p, In-3d, Zn-2p, and Se-3d core-levels were spotted and measured, respectively, as shown in Fig. 3b–e, respectively. In the Cu-2p core-level spectrum (Fig. 3b), the doublet peak at 931.9 eV and 951.7 eV corresponds to the photoelectron emission from the Cu-2p$_{3/2}$ and Cu-2p$_{1/2}$ orbitals, respectively.[38] The Cu-2p peak was analyzed (with 5-point averaging) to observe Cu(0), Cu(I), and Cu(II), and the XPS spectra are presented in Fig. S3.† Cu(I) was identified with a mild satellite peak at 945 eV, which is shown in Fig. S3† and marked with a blue circle. The Cu(II) state will give a strong satellite peak at 943 eV, which was absent in this case. However, Cu(0) will appear without any satellite peak, which was also not the case in the present situation. Therefore, Cu existed in the Cu(I) state alone and the other possibilities were ruled out. Although Cu(II) acetate was used as the starting material for the synthesis, the core-level spectrum of Cu-2p only shows the characteristics of Cu(I). The result signifies that Cu(II) was reduced to Cu(I) by the fatty amines (OLA used in this work) during the reaction carried out at a higher temperature.[39,40] As shown Fig. 3c–e, the chemical states of the In, Zn and Se elements were determined to be +3 (In 3d$_{5/2}$, 444.5 eV; In 3d$_{3/2}$, 452 eV),[41] +2 (Zn 2p$_{3/2}$, 1021.7 eV; Zn 2p$_{1/2}$, 1044.7 eV),[41] and −2 (Se 3d, 53.9 eV),[35] respectively. More importantly, the photoemission intensity of the Cu-2p and In-3d signals in the Cu^I:Zn–In–Se/ZnSe C/S NCs was weakened compared to that of the parent Cu^I:Zn–In–S core NCs, suggesting that the inter-diffusion of Zn(II) ions in the core lattice partially substituted the Cu(I) and In(III) ions during the
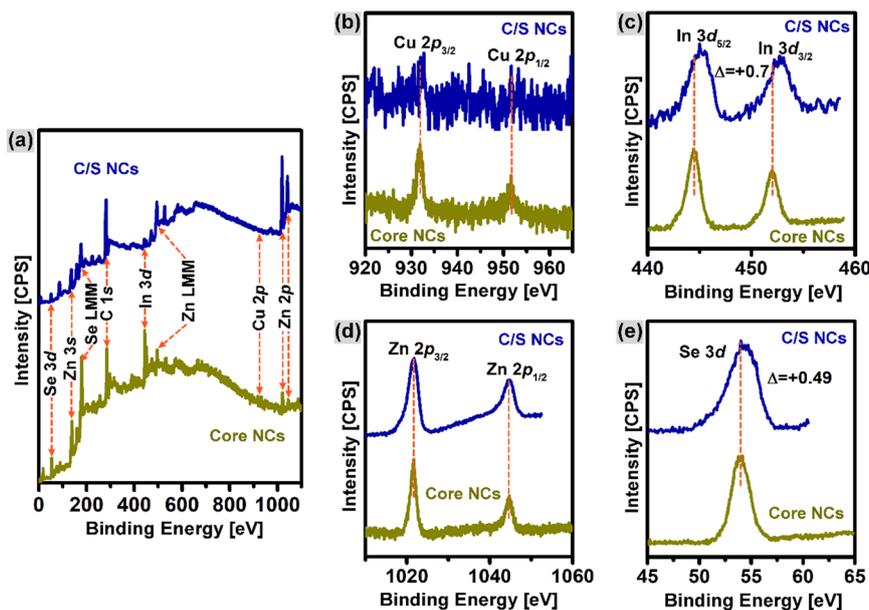
1322 | *RSC Appl. Interfaces*, 2024, **1**, 1317–1333

© 2024 The Author(s). Published by the Royal Society of Chemistry

Fig. 3 XPS spectra of Cu^I:Zn–In–Se core NCs and Cu^I:Zn–In–Se/ZnSe C/S NCs of NCs@E (0.08 mmol of Cu content). (a) Wide-scan spectra and high-resolution core-level XPS spectra for the (b) Cu 2p, (c) In 3d, (d) Zn 2p and (e) Se 3d elements.

growth process of the ZnSe shell. Although XPS presented hints regarding the cation exchange, there may be a slight difficulty in confirming it. This is because the intensity of the Cu-2p and In-3d peaks can also be reduced due to the shielding effect of the grown core layer. Therefore, this XPS intensity change is not firmly considered as evidence for the cation exchange, rather the cation exchange was strongly proven through the absorption and PL analysis, as discussed in the respective sections. Also, the In-3d and Se-3d signals show slight chemical shifts of +0.7 eV and +0.49 eV, respectively, after three series of Zn precursor injections into the core NCs, suggesting the formation of a ZnSe shell, which can impact the electronic environment in the NCs.[42] It should also be noted that the use of DDT at the employed high temperatures during synthesis can possibly cause the leaching of sulfur ions, which was checked through the XPS spectra presented in Fig. S3 of the ESI.† The peak positions were marked and no peak related to S (located at 162 eV) was found and no sulfur was observed.

To gain better information about the quantity of Cu in each sample, XPS was carried out on all the core NCs containing 0.01, 0.02, 0.04 and 0.08 mmol doped Cu ions, and only the Cu-2p peaks of these samples are presented in Fig. S4 of the ESI† and the quantification of all four NCs are presented in Table S1 of the ESI.† The Cu content in at% was found to increase with an increase in the Cu doping content in the core NCs. Increasing the Cu content can also be obvious by keen observation of the increasing intensity of the Cu-2p XPS peak in Fig. S4.†

3.3. Optical properties

The optical properties such as absorption, emission, and excited-state lifetime of the Cu^I:Zn–In–Se core and Cu^I:Zn–In–

Se/ZnSe C/S NCs are deliberated here. Fig. 4(a–e) presents the UV-vis absorption spectra of the C/S NCs together with their mother core NCs. The excitonic absorption spectra of the NCs (Fig. 4a–e) were not as clearly distinct as that in the
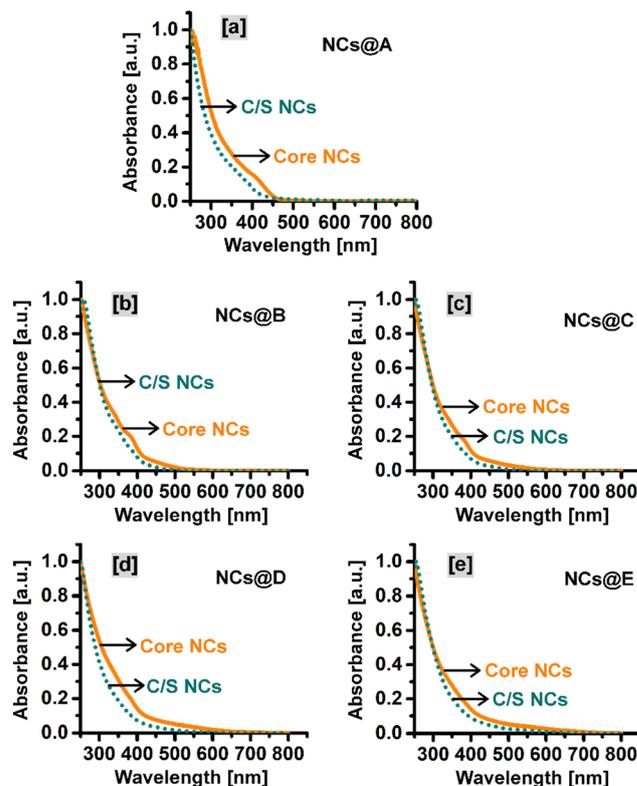

Fig. 4 Normalized UV-vis absorption spectra of core and C/S NCs. (a) Pristine Zn–In–Se/ZnSe (NCs@A) and (b–e) Cu^I:Zn–In–Se/ZnSe NCs with different Cu ion doping concentrations in the core (NCs@B to NCs@E).

© 2024 The Author(s). Published by the Royal Society of Chemistry

RSC Appl. Interfaces, 2024, **1**, 1317–1333 | **1323**

binary NCs,[29,43,44] instead they look like more or less a featureless profile with a tail elongated to a higher wavelength. This characteristic profile is partially caused by the irregular elemental distribution among the various NCs in the ensemble, which is inconsistent with the properties of these alloy NCs.[12,45] Each graph in Fig. 4 compares the absorption behavior of the core and C/S alloy NCs. In all cases, the absorption onset wavelength of the C/S NCs shifted to a lower wavelength compared to their mother core NCs. The blue-shift in the absorption peak is the reverse trend of the epitaxial growth of shell material over the initial core NCs. Reasonably, it indicates cationic inter-diffusion/ exchange between the ZnSe shell layer and Cu^I:Zn–In–Se core material during the formation of the shell, and consequently, this causes the blue-shift in the onset of absorption.[46]

The fluorescence emission spectra of all synthesized NCs are presented in Fig. 5. The pristine Zn–In–Se core NCs when excited at 320 nm show a blue emission with the wavelength maximum at 467 nm (inset image in Fig. 5a). The emission spectrum was deconvoluted using the Gaussian function by
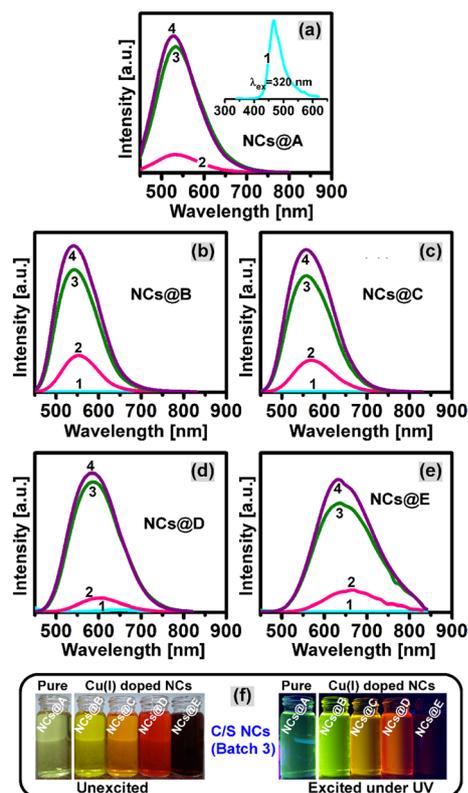
considering the types of possible radiative transitions in the host NC. The Gaussian fit, as presented in Fig. S5 of the ESI,† provides three emission components with their wavelength maxima at 464 nm, 489 nm, and 541 nm. With reference to the previous reports, the radiation observed at 464 and 489 nm is related to the Zn interstitial (Zn_i) defects and Zn vacancy (V_{Zn}), respectively.[36] The emission at 541 nm is ascribed to the indium–zinc antisite (In_{Zn}) defect emission, that is, indium atoms are substituted at the zinc site.[36] Fig. S6a of the ESI† shows the normalized fluorescence emission spectra of the pristine and Cu^I-doped Zn–In–Se alloy core NCs. One can note that on moving from the pristine Zn–In– Se NCs (NCs@A) to the heavily doped Cu^I:Zn–In–Se NCs (NCs@E), the position of the emission peak is continuously shifted to the red end of the electromagnetic spectrum from 467 to 780 nm. Notably, a very weak emission was observed from all the core NCs irrespective of doping. As shown in Fig. S6a,† the Cu ion content greatly influenced the emission property of the doped colloidal core nanocrystals. The broad photon emission of the Cu^I-doped colloidal core NCs is associated with multiple overlapping emissions by the radiative transition from the donor states (Zn_i and/or In_{Zn}) below the conduction band edge to the acceptor levels (V_{Zn} defects and/or Cu–T$_2$ state), which are located above the valence band edge.[13,37,47] The red-shift in the emission peak of the Cu^I:Zn–In–Se NCs as a function of the dopant concentration is due to the shift in the conduction band edge position by increasing the Cu ion concentration, thus tuning the emission spectrum in the visible region.[37] This shift cannot be just due to the change in the particle size given that the size change was small compared to the core nanocrystals. The emission from the Cu-doped ZnInSe QDs with varying Cu concentrations is indeed primarily due to the donor and acceptor pair (DAP) recombination facilitated by the Cu acceptor levels introduced in the QDs. This DAP recombination mechanism leads to an emission that is distinct from the band edge emission, with characteristics that depend on the Cu concentration.

Fig. 5(a–f) shows the fluorescence spectra of the five sets of Cu^I:Zn–In–Se/ZnSe C/S NCs with and without dopant in the core NCs. It can be observed that the overgrowth of the ZnSe shell by three batches of Zn(II) precursor injections on the surface of the pristine Zn–In–Se (Fig. 5a) and Cu^I:Zn–In–Se (Fig. 5b to f) core NCs resulted in a strong enhancement in the fluorescence intensity. This is attributed to the reduced density of defects and/or dangling bonds on the surface of the core NCs. Moreover, with the overgrowth of the ZnSe shell around the core NCs by the injection of the Zn(II) precursor, the emission band positions of NCs were blue-shifted from the initial emission wavelengths of 535, 557, 605, 650 and 780 nm to 528, 542, 557, 585 and 633 nm for the NCs@A, NCs@B, NCs@C, NCs@D and NCs@E samples, respectively (Table 1). The observed blue-shift in the emission spectra of C/S NCs upon the injection of the Zn(II) precursor is due to the diffusion of the smaller-sized Zn^{II} foreign cations (0.74 Å) into the already grown core NC lattice structure, filling the vacancy sites and partially replacing the

Fig. 5 Fluorescence emission spectra of the core and C/S NCs. (a) Pristine Zn–In–Se/ZnSe (NCs@A), (b–e) Cu^I:Zn–In–Se/ZnSe NCs with different Cu doping concentrations in the core (NCs@B to NCs@E). The inset graph in (a) is the emission spectrum of pristine Zn–In–Se core NCs excited at 320 nm. All the NCs were excited at 430 nm wavelength for acquiring the emission spectra except for pristine Zn– In–Se core NCs, for which the excitation wavelength was 320 nm. Note that the numbers 1, 2, 3, and 4 in the spectra represent the core, batch 1, batch 2, and batch 3 C/S NCs, respectively. (f) Photographs of unexcited and excited (under UV) colloidal solutions of the pristine and Cu^I-doped Zn–In–Se/ZnSe C/S NCs.

1324 | *RSC Appl. Interfaces*, 2024, **1**, 1317–1333

© 2024 The Author(s). Published by the Royal Society of Chemistry

Table 1 Fluorescence characteristics of the hydrophobic Cu^I:Zn–In–Se/ZnSe C/S NCs with and without dopant in their core

Sample details			
Given sample name	Dopant concentration in core NCs		Emission maximum (nm)
NCs@A	Pristine Zn–In–Se	Core	467
		Batch 1	535
		Batch 2	534
		Batch 3	528
NCs@B	Cu – 0.01 mmol	Core	557
		Batch 1	553
		Batch 2	543
		Batch 3	542
NCs@C	Cu – 0.02 mmol	Core	605
		Batch 1	570
		Batch 2	558
		Batch 3	557
NCs@D	Cu – 0.04 mmol	Core	650
		Batch 1	608
		Batch 2	587
		Batch 3	585
NCs@E	Cu – 0.08 mmol	Core	780
		Batch 1	668
		Batch 2	639
		Batch 3	633

larger Cu^I (0.96 Å) and/or In^{III} (0.81 Å) native cations, which yielded a graded ZnSe shell over the core NCs.[48,49] Ultimately, the cation exchange process contributed to the contraction of the core NCs with an inhomogeneous elemental distribution, which led to the widening of the optical bandgap energy (see Fig. 4). The diffusion of the Zn^{II} foreign cation towards the core NCs leading to cation exchange is a thermodynamically driven process. The cation exchange process, given that it exchanges cations between the core and shell, may reduce the lattice strain between them, which is normally caused by the lattice mismatch, depending on if they are homoepitaxial or hetero-epitaxially grown C/S NCs.[50] Different mechanisms for the diffusion of cations across the C/S boundary during cation exchange have been reported in the literature. In the $CsPbCl_3$/$CsMnCl_3$ C/S material system with a perovskite structure, the Mn ion diffuses from the B-site of the shell material $CsMnCl_3$ to the core material $CsPbCl_3$ to form the Mn-doped $CsMnCl_3$ core.[51] This cation diffusion is tuned by various thermal annealing of the C/S system, which led to high tunability in the PL emission and environmental stability of the $CsPbCl_3$/$CsMnCl_3$ C/S nanoparticles. The Mn doping in the core upon cation exchange creates a pathway for energy transfer, enhancing the photophysical properties of the perovskite materials. DFT calculations proved that the initial doping site or the environment is crucial for the efficient trapping of the doping ions and their further migration.[52] The role of the doping ions in various sites of perovskite-structured materials leading to changes in their optical properties is thoroughly discussed in the literature.[53] However, the dopant position and migration can be highly influenced by the local composition.[54]

The maximum observed blue-shifts in the emission band of C/S NCs induced by cation exchange during the shelling process are 7, 15, 48, 65, and 147 nm for the NCs@A, NCs@B, NCs@C, NCs@D, and NCs@E samples, respectively.

It can be observed that the shift in the wavelength (blue-shift) is directly scaled with the relative concentration of Cu doping in the core NCs. This further reveals that the Cu(I) ion has a higher rate of cation exchange with the Zn(II) ion than with the In(III) ion. Moreover, the extent of the blue-shift in the Cu^I:Zn–In–Se/ZnSe C/S NCs as a function of batch of Zn(II) precursor injection was reduced significantly, which almost reached a balance with the enhanced emission peak intensity. This signifies the formation of a binary ZnSe shell layer over the graded interface between the core and shell. In the present Cu^I:Zn–In–Se/ZnSe C/S NCs, partial cation exchange and shelling primarily occurred over the core Cu^I:Zn–In–Se NCs during the encapsulation of the ZnSe shell by serial injection of the Zn(II) precursor at a higher reaction temperature. The fluorescence spectra of the resulting C/S NCs of Cu^I:Zn–In–Se/ZnSe with and without Cu ion in the core are presented in Fig. S6b,† exhibiting a good tunable emission (Fig. S6a†). The digital snapshot of the resulting Cu^I:Zn–In–Se/ZnSe C/S NCs dissolved in chloroform solvent under UV-light excitation (Fig. 5f) shows their color tunability by emitting electromagnetic radiation in the visible region of the spectrum from green to red color. Furthermore, the relative quantum yield of NCs was measured using rhodamine 6G dye as the standard reference. The PLQY of the core NCs was determined to be 3.76%, 1.54%, 6.04%, and 3.54% for NCs@B, NCs@C, NCs@D, and NCs@E, respectively. After the ZnSe shell coating over the core NCs, their PLQY increased. The PLQY of C/S NCs was 57.95% (NCs@B), 17.5% (NCs@C), 54.1% (NCs@D), and 16.74% (NCs@E). The quantum yield was found to be quite high, and therefore this material can be effectively used in optical applications such as bioimaging and LEDs.

Besides absorption and luminescence characteristics, the trap states involved in the radiative transition of charge
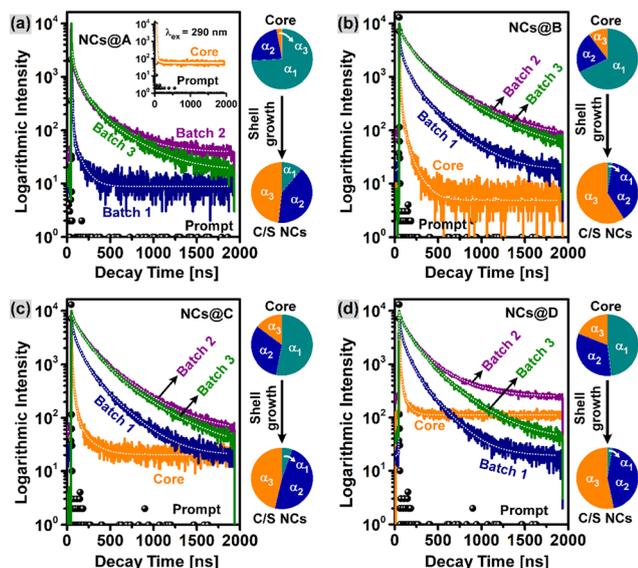
© 2024 The Author(s). Published by the Royal Society of Chemistry

RSC Appl. Interfaces, 2024, **1**, 1317–1333 | **1325**

Fig. 6 Fluorescence decay curves of pristine and Cu^I-doped Zn–In–Se/ZnSe (core and C/S with three batches of Zn-precursor injection) colloidal NCs with tri-exponential fit (white dotted lines). (a) NCs@A (pristine) (b) NCs@B (0.01 mmol of Cu), (c) NCs@C (0.02 mmol of Cu) and (d) NCs@D (0.04 mmol of Cu). The pie chart on the right side of each graph presents the amplitude fraction of three decay components (α_1, α_2 and α_3) in the core and its respective final C/S NCs (batch 3 of Zn-precursor injection).

carriers in the present NCs were studied by monitoring the emission decay mechanism using a time-correlated single photon counting (TCSPC) technique with excitation at 460 nm. Fig. 6 shows the fluorescence decay profiles of the pristine and Cu^I-doped Zn–In–Se/ZnSe core and C/S colloidal NCs acquired at their respective emission wavelengths. All the transient curves exhibit tri-exponential decay characteristics, which include a short-live decay component, τ_1, intermediate decay component, τ_2, and long-live decay component, τ_3. All the fluorescence lifetime parameters were

obtained by fitting the curves using the tri-exponential function (explained in eqn (S1), (S2), and (S3), respectively, of the ESI†) and summarized in Table 2.

The tri-exponential decay kinetics τ_1, τ_2, and τ_3 signify that various charge carrier transition pathways exist in these NCs. The faster relaxation process τ_1 with the decay lifetime lying in the range of 1.12–37.80 ns (Table 2) results from the charge carrier trapping at the surface defects, which usually have a shorter lifetime in comparison with that of deep-trap states.[55,56] The trap states at the interface of the core and shell are similar to the states at the surface of core NCs, and thus the fast relaxation process τ_1 in the case of C/S NCs is ascribed to the interface-trapped states.[51] Alternatively, the slow processes τ_2 and τ_3 are associated with the radiative transition processes that occur through both the deep defect-related donor–acceptor pair and conduction band-to-acceptor Cu–T$_2$ state, which are the main contributors to the emissions in the Cu^I:Zn–In–Se/ZnSe C/S NCs.[55,57] The values of the intermediate decay component τ_2 are in the range of 6.76–145.59 ns, while the long-live decay component τ_3 has values in the range of 60.19 ns to 396.61 ns.

According to Table 2, it can be inferred that the average fluorescence lifetime $\langle \tau_{avg} \rangle$ of the pristine and Cu^I-doped Zn–In–Se core NCs is shorter than the decay times in their respective C/S heterostructures and it progressively increases as the batch of Zn-precursor injection increases from batch 1 to batch 3. This indicates that overcoating the core NCs with a ZnSe shell can effectively reduce the contribution of the fast decay channel by eliminating the surface defect states. The prolonged average fluorescence lifetime $\langle \tau_{avg} \rangle$ from the core to shell differs for the samples. Specifically, the exciton lifetime increased from 40.2 ns to 295.2 ns for NCs@A, from 63.3 ns to 348.7 ns for NCs@B, from 99.2 ns to 324.8 ns for NCs@C, and 46.1 ns to 279.6 ns for NCs@D. Simultaneously, the average exciton lifetime of the C/S NCs is prolonged by increasing the batch number of Zn precursor injections from batch 1 to batch 3. For instance, for a set of samples in

Table 2 The tri-exponential fit parameters and average decay lifetimes were obtained by fitting the fluorescence lifetime decay profile of the colloidal NCs

Cu^I:Zn–In–Se/ZnSe C/S NCs		Tri-exponential parameters									
		τ_1 (ns)	α_1 (%)	τ_2 (ns)	α_2 (%)	τ_3 (ns)	α_3 (%)	f_1 (%)	f_2 (%)	f_3 (%)	$\langle \tau_{avg} \rangle$ (ns)
NCs@A (pristine)	Core	1.12	74.17	6.76	22.84	76.49	2.99	17.82	33.12	49.06	40.0
	Batch 1	2.36	62.11	7.56	30.10	91.09	7.79	13.53	20.99	65.48	61.5
	Batch 2	4.68	19.51	58.59	29.92	292.75	50.58	0.55	10.53	88.92	266.5
	Batch 3	15.60	11.05	96.00	40.71	344.92	48.24	0.83	18.86	80.31	295.2
NCs@B (0.01 mmol Cu)	Core	5.49	67.82	25.22	22.01	103.76	10.17	18.78	28.00	53.22	63.3
	Batch 1	6.28	10.36	70.74	37.22	279.04	52.42	0.38	15.19	84.43	246.4
	Batch 2	10.67	2.05	116.89	33.29	373.76	64.66	0.08	13.86	86.06	337.9
	Batch 3	20.59	2.46	130.24	38.60	396.46	58.94	0.18	17.67	82.15	348.7
NCs@C (0.02 mmol Cu)	Core	5.37	53.09	26.45	32.25	141.85	14.66	8.86	26.51	64.63	99.2
	Batch 1	9.39	8.43	80.77	40.69	271.81	50.88	0.46	19.11	80.43	234.1
	Batch 2	13.16	2.20	121.76	38.80	355.62	59.01	0.11	18.36	81.53	312.3
	Batch 3	37.80	5.32	145.59	48.34	396.61	46.34	0.79	27.47	71.74	324.8
NCs@D (0.04 mmol Cu)	Core	1.65	48.10	10.78	33.00	60.19	18.90	5.05	22.62	72.33	46.1
	Batch 1	8.35	9.41	68.57	40.18	225.49	50.41	0.55	19.40	80.05	193.8
	Batch 2	8.12	2.01	108.53	40.51	315.73	57.48	0.07	19.49	80.44	275.1
	Batch 3	11.93	2.50	118.69	44.20	328.30	53.30	0.13	23.04	76.83	279.6

1326 | *RSC Appl. Interfaces*, 2024, **1**, 1317–1333

© 2024 The Author(s). Published by the Royal Society of Chemistry

NCs@B, the $\langle \tau_{avg} \rangle$ was lengthened from 63.3 ns (core) to 246.4 ns when the first batch of Zn shell precursor was injected and further increased to 337.9 ns for batch 2, and it reaches to the higher value of 348.7 ns for batch 3. The Cu^I: Zn–In–Se/ZnSe C/S NC sample with 0.01 mmol Cu concentration in its core (batch 3 of NCs@B) possessed the largest average lifetime $\langle \tau_{avg} \rangle$ of 348.7 ns.

Besides, after shelling the core NCs with the ZnSe semiconductor, the fractional amplitude (in percent) of the short-lived component α_1 declined, and concurrently the contribution of the intermediate component α_2 and the long-lived component α_3 increased compared to their core NCs (Table 2). In addition, the changes in the fractional amplitude of the colloidal NCs before (core) and after injection of the Zn precursor (C/S NCs, batch 3) are represented as a pie chart on the right side of each graph in Fig. 6. It can be seen that the fractional amplitude of τ_1 for the core NCs of the pristine and Cu^I-doped Zn–In–Se with various dopant concentrations is larger than the amplitudes of τ_2 and τ_3 (α_2 and α_3, respectively), and then it was quenched significantly after shelling the core with ZnSe, while the decay amplitude fractions of τ_2 and τ_3 increased. This is a clear indication of the effective depopulation of the surface defects by the growth of the ZnSe shell layer over the core NCs. This signifies the increased rate of donor–acceptor radiative transition with the suppressed surface or interface defect states. The fractional intensities f_1, f_2 and, f_3 (Table 2) give the weights of each decay component (τ_1, τ_2, and τ_3) and signify the proportion of the excited-state population that radiatively decays through each pathway, respectively.[58] It was also noticed that the long-lived component τ_3 is largely responsible for the whole emission process in the pristine and Cu^I-doped Zn–In–Se/ZnSe C/S NCs. The optical studies suggested that the dopant and shell precursor concentrations greatly influence the optical properties of the resultant Cu^I: Zn–In–Se/ZnSe C/S NCs with improved emission intensity and prolonged fluorescence lifetime, which demonstrates the suitability of using these NCs in different applications.

For any application, quantum dots are expected to have better photostability with respect to irradiation and time.

Therefore, a photostability test was conducted using the C/S NCs containing the lowest and highest Cu content, that is 0.01 and 0.08 mmol, respectively. These C/S NCs were irradiated continuously for 24 h at the excitation wavelength of 365 nm and their PL emission spectra were acquired at specific intervals, which are presented in Fig. 7a and b, respectively. The other experimental conditions were maintained as that in the regular PL measurements. It should be noted that the PL intensity considerably decreased in both samples when continuously irradiated and the change in the relative PL intensity with respect to irradiation time is presented in Fig. 7c. The emission intensity was very stable up to the first three hours, and then subsequently decreased. However, when we looked at the absolute intensity of emission in both samples, the intensity was reduced from 3.9×10^6 to 1.6×10^6, which was stable with the same order of emission intensity maintained. The absolute intensity of emission in the 0.08 Cu-doped C/S NC decreased from 1.8×10^6 to 0.9×10^6. In this case, although a decrease in relative intensity was observed in 24 h, the absolute emission intensity remained quite high, which is sufficient for using these C/S NCs for various photo-emission applications.

3.4. Optical studies of PMMA–Cu^I:Zn–In–Se/ZnSe NC composite films

Optically transparent PMMA–Cu^I:Zn–In–Se/ZnSe NC composite films with tunable emissions were prepared by mixing the already prepared Cu^I:Zn–In–Se/ZnSe C/S NCs (batch 3), with various color-emissions at wavelengths such as 542 nm (full width at half maximum, FWHM; 93.3 nm), 557 nm (FWHM; 101.8 nm), 585 nm (FWHM; 111.7 nm) and 633 nm (FWHM; 146 nm), with a PMMA–chloroform solution. A bare PMMA film was also prepared and used as the control. Subsequently, the bare PMMA and PMMA–NC composite films were subjected to optical characterization. Fig. S7 in the ESI† displays the photographs of the PMMA–NC composite films on a glass substrate excited under ambient light and UV light and their corresponding UV-visible measurement results for optical transmittance. The top row of Fig. S7a† shows that the PMMA–
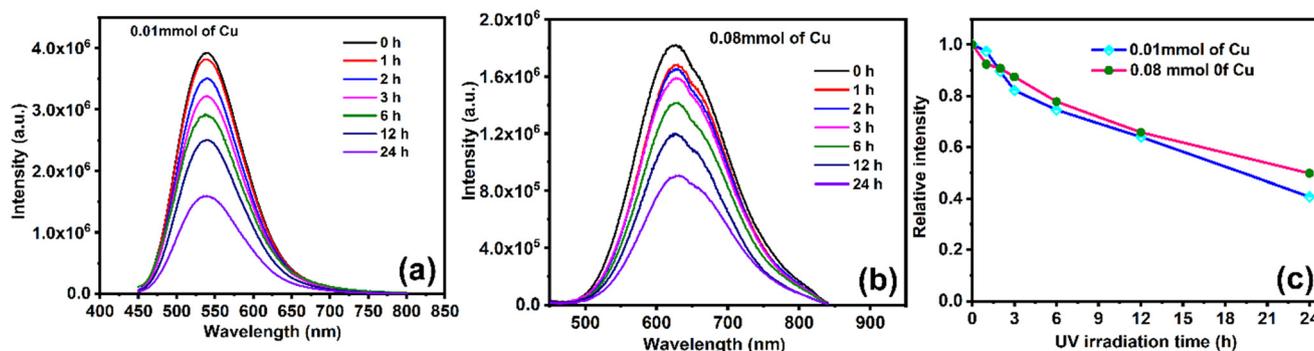

Fig. 7 PL emission spectral set for (a) 0.01 Cu- and (b) 0.08 Cu-containing C/S NCs acquired for the continuous irradiation of the NCs with 365 nm excitation wavelength for 24 h to understand the photostability of the NCs. (c) Variation in the relative intensity of the PL emission with respect to UV light irradiation for 24 h.

NC composite films are transparent and the bottom row images show that these films are highly fluorescent, obviously with the same emission color as the blended NCs. This implies that NCs were well-dispersed in the PMMA polymer matrix. According to the light transmittance curves shown in Fig. S7b,† it can be observed that the bare glass substrate and blank PMMA film have a light transmittance of ~90% and ~80%, respectively, in the visible spectral range. It is a well-known fact that green light at the wavelength of about 555 nm is much more sensitive to the human eyes. Accordingly, the optical transmittance of ~73%, 79%, 62%, and 50% were obtained at the wavelength 555 nm for the PMMA–NC composite films containing C/S NCs with various photon-emissive wavelengths such as 542, 557, 585, and 633 nm, respectively. It can be noted from the optical transmission curves that the PMMA–NC composite film with 557 nm emission showed better optical transparency than that of the other composite films. Also, it should be noted that the optical transparency of the films decreased with an increase in the emission wavelength of the NCs from 557 to 633 nm. The decrease in the visible light transparency of the PMMA–NC composite films can be mainly due to the light scattering by the aggregated particles in the film. It is also interesting to note the transmittance of the composite films was much lower than that of the bare PMMA film in the ultraviolet region (Fig. S7b†), which signifies that the prepared composite films have the capability for UV-shielding applications.

Fig. 8a–d show a comparison of the fluorescence spectra of the Cu[I]:Zn–In–Se/ZnSe NC colloidal solutions and films of the polymer–NC composite. It can be observed that the fluorescence maximum was red-shifted from the colloidal solution to the composite film and the degree of shift increased with an increase in the emission wavelength of the NCs from 542 to 633 nm. The observed degree in red-shift for PMMA–NC composite films with NCs@542 nm, NCs@557 nm, NCs@585 nm, and NCs@633 nm was 2 nm, 12 nm, 33 nm, and 70 nm, respectively. The reason for the red-shift in the fluorescence spectrum of the PMMA–NC composite films could be the aggregation-induced energy transfer from the smaller to larger NCs, as observed in the literature for nanocrystals.[59] The FWHM of the fluorescence emission peak of the NC colloidal solutions and their polymer composite solid films were compared and listed in Table S2.† It should be noted that the fluorescence peaks of the solid films were found to be broadened compared to their respective NC solutions. The highest change in the FWHM was found to be 24.5 nm, from 146.0 nm to 170.5 nm in the case of NCs@633 nm, and that for the other emission wavelength NCs is close to 4 nm. Fig. 8(e and f) show the digital images of the free-standing bare PMMA film, PMMA–NC composite films, and their emitting state under UV light exposure at the wavelength of 365 nm. Under the UV light excitation, the free-standing PMMA–NC composite films (Fig. 8e) show emitted colors in the visible region, varying from green to red. To acquire the images in Fig. 8f, the free-standing composite films were placed on a printed white paper, with the printed text "PMMA/NCs" and the image acquired under ambient light from the top side to check if the text below the film was visible. Fig. 8f shows that the printed text is clearly visible, which shows the good optical transparency of the PMMA–NC composite film in daylight. Also, the film was bent by applying manual pressure through the fingers, as shown in Fig. 8g, and it was very flexible.

3.5. Emission characteristics of hydrophilized colloidal NCs

In the optical bioimaging study, three types of Cu[I]:Zn–In–Se/ZnSe C/S NCs with different emission wavelengths such as NCs@542 nm (Batch 3 of NCs@B), NCs@557 nm (batch 3 of NCs@C) and NCs@633 nm (batch 3 of NCs@E) were selected and subjected to ligand-exchange with hydrophilic 11-MUA ligands following the procedure described in Section 2.5. Previously, the prepared C/S NCs (OLA-coated NCs) were only well dispersed in organic solvents, and therefore converting them into water-dispersible NCs is important before their use for bioimaging. The ligand-exchange was accomplished at pH ~12, yielding a high concentration of deprotonated thiolate groups (–S[−]) of 11-MUA, which exchanged the native ligands OLA on the surface of NCs, thereby making them water-dispersible. The emission property of the water-dispersible 11-MUA ligand-capped NCs is significant for their application in optical imaging, and therefore fluorescence spectroscopy measurement was carried out. Fig. S8 in the ESI† displays the fluorescence emission spectra of the Cu[I]:Zn–In–Se/ZnSe C/S

Fig. 8 (a–d) Comparison of the fluorescence spectra of Cu[I]:Zn–In–Se/ZnSe C/S NCs before (colloidal solution) and after embedding in PMMA matrix (composite film). (a) NCs@542 nm, (b) NCs@557 nm, (c) NCs@585 nm and (d) NCs@633 nm. (e) Photograph of the color-tunable PMMA–NC films under UV light excitation (365 nm wavelength). Photographs of the PMMA–NC composite films showing (f) optical transparency under ambient light excitation and (g) mechanical stability and flexibility of the composite films under manual pressure given by hands.

1328 | *RSC Appl. Interfaces*, 2024, **1**, 1317–1333

© 2024 The Author(s). Published by the Royal Society of Chemistry

NCs with various dopant contents before and after ligand-exchange with 11-MUA and their emission profiles were compared. As seen from the fluorescence emission spectra, the peak profiles of the C/S NCs remained intact even after ligand-exchange with 11-MUA, but underwent a slight peak shift. The fluorescence peak was shifted by about 7 nm (red-shift) for NCs@542 nm, 3 nm (red-shift) for NCs@557 nm, and 3 nm (blue-shift) for NCs@633 nm, which is quite small. The digital photographs presented below each fluorescence spectrum of the NCs in Fig. S8† show three representative colloidal NCs such as NCs@542 nm, NCs@557 nm and NCs@633 nm under UV light exposure. In chloroform, the NCs remained at the bottom of the container, whereas they moved to the top surface of the solution after ligand exchange and become water dispersible. The digital pictures demonstrate that the emission colour of the NCs in both organic solvent (hydrophobic) and water phase (hydrophilic) are nearly identical.

3.6. *In vitro* fluorescence imaging and cytotoxicity studies

To further verify the application prospect of the hydrophilized Cu^{I}:Zn–In–Se/ZnSe C/S NCs in biological imaging, an *in vitro* cell imaging study was assessed on human HEK293 and HeLa cells, which were separately co-incubated with hydrophilized NCs of NCs@542 nm, NCs@557 nm and NCs@633 nm (procedure is presented in Section 2.7). To validate the effective cellular uptake of the hydrophilized NCs, the treated cell lines were scanned by a laser scanning confocal microscope excited with a 405 nm laser. Fig. 9a and b show the confocal images of the NC-treated HEK293 and HeLa cells, acquired with a 20× objective lens, respectively. In both figures, the left row shows the bright field image, the middle row shows the fluorescence image acquired under 405 nm laser excitation, and the right row presents the overlay image of the bright field and fluorescence images. The morphological characteristics of the tested cells were observed clearly in the bright-field optical images. As seen in the fluorescence images, the NC-treated cells were brightened with various colors because of the luminescence from the NCs under the excitation of the 405 nm laser and exhibited green (top image), yellow (middle image), and red (bottom image) fluorescence corresponding to the NCs@542 nm, NCs@557 nm, and NCs@633 nm samples, respectively. When the fluorescence images of both
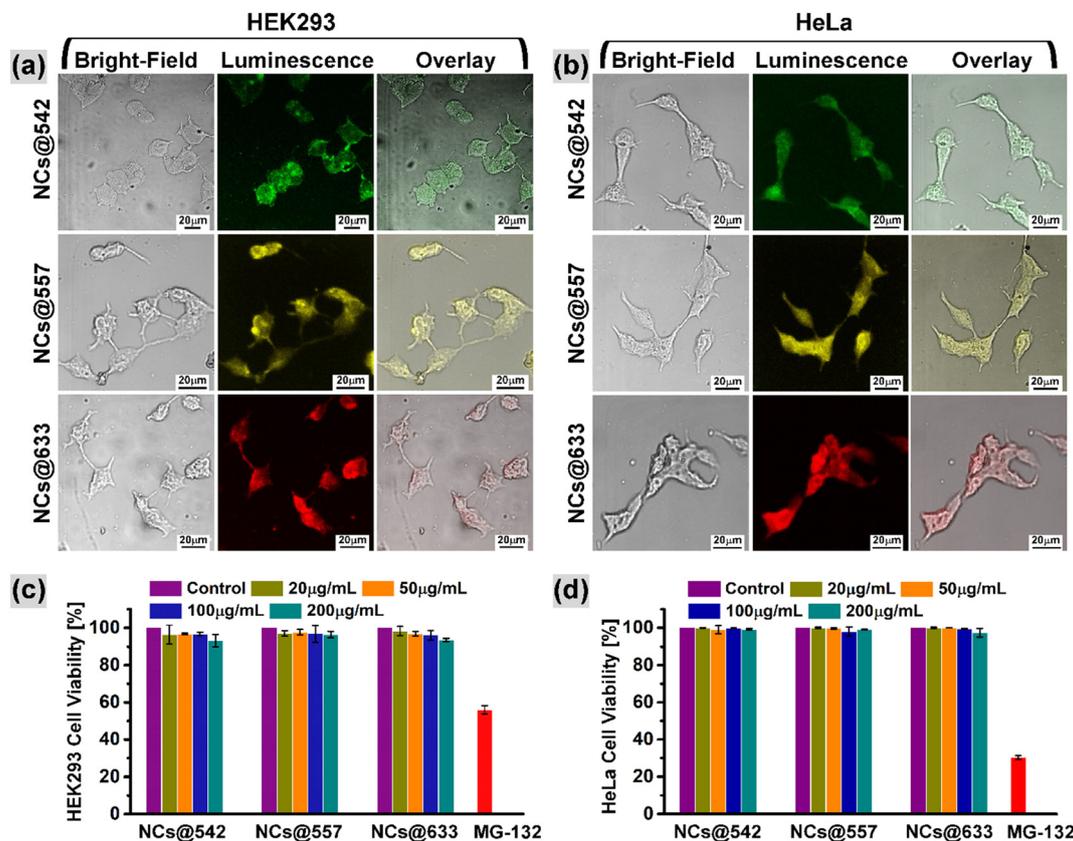

Fig. 9 Laser scanning confocal microscopy images of (a) HEK293 and (b) HeLa cells treated with hydrophilized Cu^{I}:Zn–In–Se/ZnSe C/S NCs. In both (a) and (b), the left column shows the bright-field images, the centre column shows the luminescence images acquired with an excitation wavelength of 405 nm and the right column is the overlay images produced by overlapping the bright-field and luminescence images. The concentration used for the bioimaging study is 100 μg mL^{-1} and the incubation time is 6 h. The cytotoxicity study, as evaluated by the reduction in metabolic activity (survival rate), of the hydrophilized Cu^{I}:Zn–In–Se/ZnSe C/S NC-treated (c) HEK293 and (d) HeLa cells relative to the control (PBS). The incubation time was 48 h. All the data are shown as average ±SD (*n* = 3).

© 2024 The Author(s). Published by the Royal Society of Chemistry

RSC Appl. Interfaces, 2024, **1**, 1317–1333 | **1329**

cells were merged with their corresponding bright-field images, that is, overlay image, as shown in Fig. 9a and b, it became evident that the observed luminescence signals originated from within the cells. This implies the uptake of the hydrophilized NCs by the tested HEK293 and HeLa cells. The acquired optical images demonstrated that the tested cells could efficiently be probed with the eco-friendly C/S NCs synthesized in this work through visible light-prompted luminescence imaging.

Further, the cytotoxicity of the hydrophilized NCs@542 nm, NCs@557 nm, and NCs@633 nm samples against HEK293 and HeLa cells was evaluated by measuring the cellular metabolic activity through the MTT assay. The *in vitro* cell viability was measured after 48 h of incubation with each NC at various concentrations ranging from 0 to 200 μg mL^{-1}. The quantification of the formazan crystals by spectroscopy (optical density, OD) corresponds to the survival rate of the NC-treated HEK293 and HeLa cells, as shown in Fig. 9c and d, respectively. The results demonstrate that the survival rate of the tested cells remained at a high level of above 93% and no obvious reduction was observed over the entire tested concentration ranges of the three various hydrophilized samples during 48 h incubation time. The hydrophilized NCs@542 nm, NCs@557 nm, and NCs@633 nm sample-treated cells exhibited a relative survival rate of over 96.7%, 96.8%, and 96.1%, respectively, towards the HEK293 cells with respect to the control at a dosage of 100 μg mL^{-1} NCs. Alternatively, the survival rate of HeLa cells at 100 μg mL^{-1} concentration of NCs decreased by 0.2%, 2%, and 0.5% (overall cell viability was above 97%) for the NCs@542 nm, NCs@557 nm, and NCs@633 nm samples, respectively. It should be mentioned that this specific concentration, that is, 100 μg mL^{-1}, of the hydrophilized samples was used as a fluorescent agent in the optical bioimaging study, which was discussed in the previous section. Thus, the cytotoxicity study proved the biocompatibility of the designed hydrophilized Cu^I:Zn–In–Se/ZnSe C/S NCs.

4. Conclusions

The eco-friendly blue-to-red tunable color emissive core/shell NCs of Cu^I:Zn–In–Se/ZnSe were synthesized *via* a one-pot organometallic colloidal method, in which the phosphine-free, highly reactive alkylammonium selenide was used as the Se precursor. The fluorescence emission results demonstrated that the content of the dopant ion Cu played the main role in tuning the emission wavelength of the Cu^I-doped Zn–In–Se alloy core NCs in the wavelength range of 467 to 780 nm. As shelling progressed with the ZnSe chalcogenide, the emissions of the resulting colloidal NCs were strongly enhanced, accompanied by blue-shifts in the wavelength position caused by the cation exchange. Also, the ZnSe shelling process further extended the fluorescence lifetimes of the NCs, and the average fluorescence lifetime of the Cu^I:Zn–In–Se/ZnSe C/S NC system was in the range of 250 ns to 350 ns. Also, green, yellow, orange, and red color emissive PMMA–NC composite flexible films were

successfully prepared *via* the drop-casting method. The developed composite films showed good transparency in the visible range, appreciable mechanical flexibility and good emission characteristics. Also, the results encouragingly suggested that the Cu^I:Zn–In–Se/ZnSe NCs incorporated in the PMMA matrix have potential to be employed as emissive materials in flexible optoelectronic applications. Moreover, the hydrophilized 11-mercaptoundecanoic acid-coated Cu^I:Zn–In–Se/ZnSe C/S NCs prepared by the ligand exchange method were applied as a luminescent agent for optical live-cell imaging in HEK-293 and HeLa cells. Both cells showed the uptake of these NCs. The cytotoxicity study revealed the minimum suppression of cell viability under the tested NC concentrations of up to 200 μg mL^{-1}. In summary, the findings of this research suggest that the prepared eco-friendly C/S NCs of Cu^I:Zn–In–Se/ZnSe featuring tunable visible light emission by dopant concentration have potential application in various fields as a luminescent material, especially in flexible electronics and bioimaging.

Data availability

The datasets used and/or analyzed during the current study are available from the corresponding author on reasonable request.

Additional information

Correspondence and requests for materials should be addressed to P. Thangadurai.

Author contributions

All authors reviewed the manuscript.

Conflicts of interest

The authors declare no competing interests.

Acknowledgements

References

1 C. R. Kagan, E. Lifshitz, E. H. Sargent and D. V. Talapin, Building Devices from Colloidal Quantum Dots, *Science*, 2016, **353**, aac5523, DOI: **10.1126/science.aac5523**.

2   S. Y. Bang, Y. H. Suh, X. B. Fan, D. W. Shin, S. Lee, H. W. Choi, T. H. Lee, J. Yang, S. Zhan, W. Harden-Chaters, C. Samarakoon, L. G. Occhipinti, S. D. Han, S. M. Jung and J. M. Kim, Technology Progress on Quantum Dot Light-Emitting Diodes for next-Generation Displays, *Nanoscale Horiz.*, 2021, **6**(2), 68–77, DOI: **10.1039/D0NH00556H**.

3   Y. Wang, R. Hu, G. Lin, I. Roy and K. T. Yong, Functionalized Quantum Dots for Biosensing and Bioimaging and Concerns on Toxicity, *ACS Appl. Mater. Interfaces*, 2013, **5**(8), 2786–2799, DOI: **10.1021/am302030a**.

4   Y. Zhou, H. Zhao, D. Ma and F. Rosei, Harnessing the Properties of Colloidal Quantum Dots in Luminescent Solar Concentrators, *Chem. Soc. Rev.*, 2018, **47**(15), 5866–5890, DOI: **10.1039/C7CS00701A**.

5   L. Tan, Y. Zhou, F. Ren, D. Benetti, F. Yang, H. Zhao, F. Rosei, M. Chaker and D. Ma, Ultrasmall PbS Quantum Dots: A Facile and Greener Synthetic Route and Their High Performance in Luminescent Solar Concentrators, *J. Mater. Chem. A*, 2017, **5**(21), 10250–10260, DOI: **10.1039/C7TA01372H**.

6   H. Tavakoli Dastjerdi, P. Qi, Z. Fan and M. M. Tavakoli, Cost-Effective and Semi-Transparent PbS Quantum Dot Solar Cells Using Copper Electrodes, *ACS Appl. Mater. Interfaces*, 2020, **12**(1), 818–825, DOI: **10.1021/acsami.9b18487**.

7   A. Sahu, A. Garg and A. Dixit, A Review on Quantum Dot Sensitized Solar Cells: Past, Present and Future towards Carrier Multiplication with a Possibility for Higher Efficiency, *Sol. Energy*, 2020, **203**, 210–239, DOI: **10.1016/j.solener.2020.04.044**.

8   S. V. Kershaw, L. Jing, X. Huang, M. Gao and A. L. Rogach, Materials Aspects of Semiconductor Nanocrystals for Optoelectronic Applications, *Mater. Horiz.*, 2017, **4**(2), 155–205, DOI: **10.1039/C6MH00469E**.

9   R. Guo, M. Zhang, J. Ding, A. Liu, F. Huang and M. Sheng, Advances in Colloidal Quantum Dot-Based Photodetectors, *J. Mater. Chem. C*, 2022, **10**(19), 7404–7422, DOI: **10.1039/D2TC00219A**.

10 A. C. Berends, M. J. J. Mangnus, C. Xia, F. T. Rabouw and C. De Mello Donega, Optoelectronic Properties of Ternary I-III-VI₂ Semiconductor Nanocrystals: Bright Prospects with Elusive Origins, *J. Phys. Chem. Lett.*, 2019, **10**(7), 1600–1616, DOI: **10.1021/acs.jpclett.8b03653**.

11 N. Tsolekile, S. Parani, M. C. Matoetoe, S. P. Songca and O. S. Oluwafemi, Evolution of Ternary I–III–VI QDs: Synthesis, Characterization and Application, *Nano-Struct. Nano-Objects*, 2017, **12**, 46–56, DOI: **10.1016/j.nanoso.2017.08.012**.

12 S. Mukherjee, J. Selvaraj and T. Paramasivam, Ag-Doped ZnInS/ZnS Core/Shell Quantum Dots for Display Applications, *ACS Appl. Nano Mater.*, 2021, **4**(10), 10228–10243, DOI: **10.1021/acsanm.1c01720**.

13 S. Cao, W. Ji, J. Zhao, W. Yang, C. Li and J. Zheng, Color-Tunable Photoluminescence of Cu-Doped Zn–In–Se Quantum Dots and Their Electroluminescence Properties, *J. Mater. Chem. C*, 2016, **4**(3), 581–588, DOI: **10.1039/C5TC04019A**.

14 W. J. Zhang, C. Y. Pan, F. Cao, H. Wang and X. Yang, Bright Violet-to-Aqua-Emitting Cadmium-Free Ag-Doped Zn-Ga-S Quantum Dots with High Stability, *Chem. Commun.*, 2018, **54**(33), 4176–4179, DOI: **10.1039/C8CC01293H**.

15 C. Wang, S. Xu, Y. Shao, Z. Wang, Q. Xu and Y. Cui, Synthesis of Ag Doped ZnInSe Ternary Quantum Dots with Tunable Emission, *J. Mater. Chem. C*, 2014, **2**(26), 5111–5115, DOI: **10.1039/C4TC00601A**.

16 J. Selvaraj, A. Mahesh, V. Baskaralingam, A. Dhayalan and T. Paramasivam, Organic-to-Water Dispersible Mn:ZnS–ZnS Doped Core–Shell Quantum Dots: Synthesis, Characterization and Their Application towards Optical Bioimaging and a Turn-off Fluorosensor, *New J. Chem.*, 2019, **43**(30), 11912–11925, DOI: **10.1039/C9NJ02222H**.

17 M. Liu, W. Yao, C. Li, Z. Wu and L. Li, Tuning Emission and Stokes Shift of CdS Quantum Dots via Copper and Indium Co-Doping, *RSC Adv.*, 2015, **5**(1), 628–634, DOI: **10.1039/C4RA11349G**.

18 H. Wang, J. Hu, M. Zhu, Y. Li, H. Qian, X. Shen, F. Liebner and T. Rosenau, Full-Color-Emitting (CuInS₂)ZnS-Alloyed Core/Shell Quantum Dots with Trimethoxysilyl End-Capped Ligands Soluble in an Ionic Liquid, *RSC Adv.*, 2019, **9**(44), 25576–25582, DOI: **10.1039/C9RA03066B**.

19 W. K. Bae, L. A. Padilha, Y. S. Park, H. McDaniel, I. Robel, J. M. Pietryga and V. I. Klimov, Controlled Alloying of the Core–Shell Interface in CdSe/CdS Quantum Dots for Suppression of Auger Recombination, *ACS Nano*, 2013, **7**(4), 3411–3419, DOI: **10.1021/nn4002825**.

20 H. Lu, Z. Hu, W. Zhou, J. Wei, W. Zhang, F. Xie and R. Guo, Synthesis and Structure Design of I-III-VI Quantum Dots for White Light-Emitting Diodes, *Mater. Chem. Front.*, 2022, **6**(4), 418–429, DOI: **10.1039/D1QM01452H**.

21 X. Kang, Y. Yang, L. Huang, Y. Tao, L. Wang and D. Pan, Large-Scale Synthesis of Water-Soluble CuInSe₂/ZnS and AgInSe₂/ZnS Core/Shell Quantum Dots, *Green Chem.*, 2015, **17**, 4482–4488, DOI: **10.1039/C5GC00908A**.

22 W.-J. Zhang, C.-Y. Pan, F. Cao and X. Yang, White-Light-Emitting Cu,Mn Co-Doped Zn–In–S/ZnS Quantum Dots with High Stability and Their Electroluminescence, *J. Mater. Chem. C*, 2017, **5**(40), 10533–10542, DOI: **10.1039/C7TC03226A**.

23 T. Omata, K. Nose and S. Otsuka-Yao-Matsuo, Fabrication of Core–Shell-Type Copper Indium Selenide and Zinc Selenide Composite Quantum Dots and Their Optical Properties, *J. Nanosci. Nanotechnol.*, 2011, **11**(6), 4815–4823, DOI: **10.1166/jnn.2011.4181**.

24 Q.-H. Zhang, Y. Tian, C.-F. Wang and S. Chen, Construction of Ag-Doped Zn–In–S Quantum Dots toward White LEDs and 3D Luminescent Patterning, *RSC Adv.*, 2016, **6**(53), 47616–47622, DOI: **10.1039/C6RA05689J**.

25 T.-T. Xuan, J.-Q. Liu, C.-Y. Yu, R.-J. Xie and H.-L. Li, Facile Synthesis of Cadmium-Free Zn-In-S:Ag/ZnS Nanocrystals for Bio-Imaging, *Sci. Rep.*, 2016, **6**(1), 24459, DOI: **10.1038/srep24459**.

26 W. J. Zhang, C. Y. Pan, F. Cao, H. Wang and X. Yang, Highly Bright and Stable White-Light-Emitting Cadmium-Free Ag,

Mn Co-Doped Zn-In-S/ZnS Quantum Dots and Their Electroluminescence, *J. Mater. Chem. C*, 2018, **6**(38), 10233–10240, DOI: **10.1039/C8TC03742F**.

27 J. Zhu, S. Mei, W. Yang, G. Zhang, Q. Chen, W. Zhang and R. Guo, Tunable Emission of Cu(Mn)-Doped ZnInS Quantum Dots via Dopant Interaction, *J. Colloid Interface Sci.*, 2017, **506**, 27–35, DOI: **10.1016/j.jcis.2017.06.043**.

28 G. Huang, C. Wang, X. Xu and Y. Cui, An Optical Ratiometric Temperature Sensor Based on Dopant-Dependent Thermal Equilibrium in Dual-Emitting Ag&Mn: ZnInS Quantum Dots, *RSC Adv.*, 2016, **6**(63), 58113–58117, DOI: **10.1039/C6RA06293H**.

29 J. Selvaraj, A. Mahesh, V. Asokan, V. Baskaralingam, A. Dhayalan and T. Paramasivam, Phosphine-Free, Highly Emissive, Water-Soluble Mn:ZnSe/ZnS Core–Shell Nanorods: Synthesis, Characterization, and in Vitro Bioimaging of HEK293 and HeLa Cells, *ACS Appl. Nano Mater.*, 2018, **1**, 371–383, DOI: **10.1021/acsanm.7b00218**.

30 L. M. Grimm, A. L. Goldberg, G. G. Poirier, L. M. Schwartz and B. A. Osborne, Proteasomes Play an Essential Role in Thymocyte Apoptosis, *EMBO J.*, 1996, **15**(15), 3835–3844, PMID: 8670888.

31 N. S. Nath, I. Bhattacharya, A. G. Tuck, D. I. Schlipalius and P. R. Ebert, Mechanisms of Phosphine Toxicity, *J. Toxicol.*, 2011, 494168, DOI: **10.1155/2011/494168**.

32 B. Stewart, A. Harriman and L. J. Higham, Predicting the Air Stability of Phosphines, Organometallics, *Organometallics*, 2011, **30**, 5338–5343, DOI: **10.1021/om200070a**.

33 J. F. L. Lox, Z. Dang, V. M. Dzhagan, D. Spittel, B. Martín-García, I. Moreels, D. R. T. Zahn and V. Lesnyak, Near-Infrared Cu-In-Se-Based Colloidal Nanocrystals via Cation Exchange, *Chem. Mater.*, 2018, **30**(8), 2607–2617, DOI: **10.1021/acs.chemmater.7b05187**.

34 Y. Liu, D. Yao, L. Shen, H. Zhang, X. Zhang and B. Yang, Alkylthiol-Enabled Se Powder Dissolution in Oleylamine at Room Temperature for the Phosphine-Free Synthesis of Copper-Based Quaternary Selenide Nanocrystals, *J. Am. Chem. Soc.*, 2012, **134**(17), 7207–7210, DOI: **10.1021/ja300064t**.

35 S. Cao, W. Ji, J. Zhao, W. Yang, C. Li and J. Zheng, Color-Tunable Photoluminescence of Cu-Doped Zn–In–Se Quantum Dots and Their Electroluminescence Properties, *J. Mater. Chem. C*, 2016, **4**, 581–588, DOI: **10.1039/C5TC04019A**.

36 X. Dong, J. Xu, X. Zhang, S. Shi, H. Yang, Z. Mo, L. Li and S. Yin, Investigating Photoluminescence Mechanism of Cu-Doped Zn–In–Se Quantum Dots by Zn/In Ratio, *J. Phys. Chem. C*, 2017, **121**(31), 16978–16984, DOI: **10.1021/acs.jpcc.7b04327**.

37 M. Kaur, A. Sharma, M. Olutas, O. Erdem, A. Kumar, M. Sharma and H. V. Demir, Cd-Free Cu-Doped ZnInS/ZnS Core/Shell Nanocrystals: Controlled Synthesis And Photophysical Properties, *Nanoscale Res. Lett.*, 2018, **13**(1), 182, DOI: **10.1186/s11671-018-2599-x**.

38 G. Chen, Q. Du, H. Zhang, R. Niu, W. Yuan, X. Xie, T. Guo and G. Liu, Cu-Related Defects and Optical Properties in

Copper–Indium–Selenide Quantum Dots by a Green Synthesis, *J. Appl. Phys.*, 2022, **131**(14), 145704(1–8), DOI: **10.1063/5.0085492**.

39 J.-J. Wang, Y.-Q. Wang, F.-F. Cao, Y.-G. Guo and L.-J. Wan, Synthesis of Monodispersed Wurtzite Structure CuInSe₂ Nanocrystals and Their Application in High-Performance Organic−Inorganic Hybrid Photodetectors, *J. Am. Chem. Soc.*, 2010, **132**(35), 12218–12221, DOI: **10.1021/ja1057955**.

40 S. Sarkar, N. S. Karan and N. Pradhan, Ultrasmall Color-Tunable Copper-Doped Ternary Semiconductor Nanocrystal Emitters, *Angew. Chem.*, 2011, **123**(27), 6189–6193, DOI: **10.1002/anie.201101572**.

41 Z. Leng, L. Huang, F. Shao, Z. Lv, T. Li, X. Gu and H. Han, Facile Synthesis of Cu–In–Zn–S Alloyed Nanocrystals with Temperature-Dependent Photoluminescence Spectra, *Mater. Lett.*, 2014, **119**, 100–103, DOI: **10.1016/j.matlet.2013.12.109**.

42 K. Wang, Z. Liang, J. Li, X. Xu, X. Cheng, H. Jin, D. Xu and G. Xu, Formation and Photoluminescence Properties of Colloidal ZnCuIn(SeₓS₁₋ₓ)₂/ZnS Nanocrystals with Gradient Composition, *J. Mater. Sci.*, 2019, **54**(3), 2037–2048, DOI: **10.1007/s10853-018-2948-2**.

43 R. Zeng, T. Zhang, G. Dai and B. Zou, Highly Emissive, Color-Tunable, Phosphine-Free Mn:ZnSe/ZnS Core/Shell and Mn:ZnSeS Shell-Alloyed Doped Nanocrystals, *J. Phys. Chem. C*, 2011, **115**(7), 3005–3010, DOI: **10.1021/jp111288h**.

44 S. L. Zhang, C. F. Lin, Y. L. Weng, L. C. He, T. L. Guo, Y. A. Zhang and X. T. Zhou, Facile and Green Synthesis of Core–Shell ZnSe/ZnS Quantum Dots in Aqueous Solution, *J. Mater. Sci.: Mater. Electron.*, 2018, **29**(19), 16805–16814, DOI: **10.1007/s10854-018-9775-8**.

45 D. Yao, H. Liu, Y. Liu, C. Dong, K. Zhang, Y. Sheng, J. Cui, H. Zhang and B. Yang, Phosphine-Free Synthesis of Ag-In-Se Alloy Nanocrystals with Visible Emissions, *Nanoscale*, 2015, **7**(44), 18570–18578, DOI: **10.1039/C5NR04856G**.

46 X. Yuan, R. Ma, J. Hua, Y. Liu, J. Li, W. Zhang, J. Zhao and H. Li, Thermal Stability of Photoluminescence in Cu-Doped Zn–In–S Quantum Dots for Light-Emitting Diodes, *Phys. Chem. Chem. Phys.*, 2016, **18**(16), 10976–10982, DOI: **10.1039/C6CP00240D**.

47 X. Dong, J. Xu, H. Yang, X. Zhang, Z. Mo, S. Shi, L. Li and S. Yin, Effect of Ligand Exchange on the Photoluminescence Properties of Cu-Doped Zn-In-Se Quantum Dots, *J. Electron. Mater.*, 2018, **47**(4), 2241–2248, DOI: **10.1007/s11664-017-6050-3**.

48 J. Ke, X. Li, Q. Zhao, Y. Shi and G. A. Chen, Novel Approach to Synthesize Ultrasmall Cu Doped Zn–In–Se Nanocrystal Emitters in a Colloidal System, *Nanoscale*, 2014, **6**(6), 3403–3409, DOI: **10.1039/C3NR06168J**.

49 A. Zhang, C. Dong, L. Li, J. Yin, H. Liu, X. Huang and J. Ren, Non-Blinking (Zn)CuInS/ZnS Quantum Dots Prepared by In Situ Interfacial Alloying Approach, *Sci. Rep.*, 2015, **5**(1), 15227(1–13), DOI: **10.1038/srep15227**.

50 H. Dong, L. D. Sun, L. D. Li, R. Si, R. Liu and C. H. Yan, Selective Cation Exchange Enabled Growth of Lanthanide Core/Shell Nanoparticles with Dissimilar Structure, *J. Am. Chem. Soc.*, 2017, **139**, 18492–18495, DOI: **10.1021/jacs.7b11836**.

1332 | *RSC Appl. Interfaces*, 2024, **1**, 1317–1333

© 2024 The Author(s). Published by the Royal Society of Chemistry

51   S. Li, H. Lin, C. Chu, C. Martin, W. MacSwain, R. W. Meulenberg, J. M. Franck, A. Chakraborty and W. Zheng, Interfacial B-Site Ion Diffusion in All-Inorganic Core/Shell Perovskite Nanocrystals, *ACS Nano*, 2023, **17**, 22467–22477, DOI: **10.1021/acsnano.3c05876**.

52   C. Chu, E. Hofman, C. Gao, S. Li, H. Lin, W. MacSwain, J. M. Franck, R. W. Meulenberg, A. Chakraborty and W. Zheng, Inserting an "atomic trap" for directional dopant migration in core/multi-shell quantum dots, *Chem. Sci.*, 2023, **14**, 14115–14123, DOI: **10.1039/d3sc04165d**.

53   A. H. Davis and W. Zheng, Discrete composition control of two-dimensional morphologic all-inorganic metal halide perovskite nanocrystals, *J. Energy Chem.*, 2021, **59**, 257–275, DOI: **10.1016/j.jechem.2020.10.023**.

54   E. Hofman, A. Khammang, J. T. Wright, Z.-J. Li, P. F. McLaughlin, A. H. Davis, J. M. Franck, A. Chakraborty, R. W. Meulenberg and W. Zheng, Decoupling and Coupling of the Host–Dopant Interaction by Manipulating Dopant Movement in Core/Shell Quantum Dots, *J. Phys. Chem. Lett.*, 2020, **11**, 5992–5999, DOI: **10.1021/acs.jpclett.0c01861**.

55   J. Seo, S. Raut, M. Abdel-Fattah, Q. Rice, B. Tabibi, R. Rich, R. Fudala, I. Gryczynski, Z. Gryczynski, W.-J. Kim, S. Jung and R. Hyun, Time-Resolved and Temperature-Dependent Photoluminescence of Ternary and Quaternary Nanocrystals of $CuInS_2$ with ZnS Capping and Cation Exchange, *J. Appl. Phys.*, 2013, **114**(9), 094310, DOI: **10.1063/1.4820269**.

56   S. Chen, V. Demillo, M. Lu and X. Zhu, Preparation of Photoluminescence Tunable Cu-Doped $AgInS_2$ and $AgInS_2$/ZnS Nanocrystals and Their Application as Cellular Imaging Probes, *RSC Adv.*, 2016, **6**(56), 51161–51170, DOI: **10.1039/C6RA09494E**.

57   W.-D. Xiang, H.-L. Yang, X.-J. Liang, J.-S. Zhong, J. Wang, L. Luo and C.-P. Xie, Direct Synthesis of Highly Luminescent Cu–Zn–In–S Quaternary Nanocrystals with Tunable Photoluminescence Spectra and Decay Times, *J. Mater. Chem. C*, 2013, **1**(10), 2014, DOI: **10.1039/C2TC00493C**.

58   Q. Wu, C. Cai, L. Zhai, J. Wang, F. Kong, Y. Yang, L. Zhang, C. Zou and S. Huang, Zinc Dopant Inspired Enhancement of Electron Injection for $CuInS_2$ Quantum Dot-Sensitized Solar Cells, *RSC Adv.*, 2017, **7**(63), 39443–39451, DOI: **10.1039/C7RA06659G**.

59   C. D. Weerd, L. Gomez, H. Zhang, W. J. Buma, G. Nedelcu, M. V. Kovalenko and T. Gregorkiewicz, Energy Transfer between Inorganic Perovskite Nanocrystals, *J. Phys. Chem. C*, 2016, **120**, 13310–13315, DOI: **10.1021/acs.jpcc.6b04768**.